DOI: 10.1002/((please add manuscript number))

Article type: Communication

Ruthenium-Based Single Atom Alloy with High Electrocatalytic Activity for Hydrogen Evolution

Cui-Hong Chen, Deyao Wu, Zhe Li, Rui Zhang, Chun-Guang Kuai, Xue-Ru Zhao, Cun-Ku Dong, Shi-Zhang Qiao, Hui Liu, and Xi-Wen Du**

C. Chen, D. Wu, Dr. Z. Li, Dr. R. Zhang, Dr. C. Kuai, Prof. C. Dong, Prof. H. Liu, Prof. X. Du, Prof. S. Qiao

Institute of New-Energy Materials

School of Materials Science and Engineering

Key Laboratory for Advanced Ceramics and Machining

Technology of Ministry of Education

Tianjin University

Tianjin 300072, China

E-mail: hui_liu@tju.edu.cn; xwdu@tju.edu.cn

Prof. S. Qiao

School of Chemical Engineering

The University of Adelaide

Adelaide, SA 5005, Australia

Keywords: single-atom alloys, hydrogen evolution reaction, pulsed laser ablation, electrocatalyst, synergistic effect

Highly efficient and stable catalysts for hydrogen evolution reaction (HER), especially in alkaline conditions is very crucial for the practical demands of electrochemical water splitting. Here, we report the synthesis of a novel RuAu single-atom alloy (SAA) by laser ablation in liquid (LAL). The SAA exhibits a high stability and a low overpotential, 24 mV@10 mA cm^{-2}, which is much lower than that of Pt/C catalyst (46 mV) in alkaline media. Moreover, the turnover frequency of RuAu SAA is 3 times that of Pt/C catalyst. Density functional theory computation indicates the excellent catalytic activity of RuAu SAAs originates from the relay catalysis of Ru and Au active sites. Our work opens a new avenue towards high-performance SAAs via fast quenching of immiscible metals.

1. Introduction

Electrochemical water splitting is an effective way to convert electric energy into clean and renewable hydrogen with high energy density, where active catalysts are very crucial to realize highly efficient conversion at a low overpotential.[1-5] So far, Pt is regarded as the most effective catalyst for hydrogen evolution reaction (HER) in acidic media, because of its appropriate adsorption of H atoms.[6,7] However, the catalysts for oxygen evolution reaction (OER) on the counter electrode are mainly composed of oxides which remain stable merely in basic or neutral conditions, and in these media, the performance of Pt-based catalysts is

dramatically depressed.[8-10] In theory, HER in basic or neutral media involves water dissociation and then hydrogen evolution, and the first step is much sluggish, leading to the conversion efficiency about two or three orders of magnitude lower than that in acidic media.[11-13] Consequently, it remains a big challenge to fabricate HER catalysts with high performance and low price for working in alkaline solution.

Ruthenium, as a member of platinum-group metals with 1/30 price of Pt,[14] has been proved to be a promising catalyst for HER in alkaline solution due to its high efficiency on water dissociation,[15-18] however, the strong interaction between Ru and H atoms impedes the subsequent hydrogen evolution because of the well-known scaling relationship for heterogeneous catalysts.[17,19-21] Many efforts had been devoted to constructing Ru-based heterostructures (e.g. Ru/carbon quantum dots,[22] Ru/C_2N,[18] RuCo/nitrogen-doped graphene,[23] fcc-$Ru/C_3N_4/C$,[17] Ru/nitrogen-doped carbon,[24] Ru/graphene[25]), which show great advantages on promoting water dissociation by synergistic effect. Nevertheless, less attention was paid on the improvement of hydrogen adsorption. Recently, single-atom alloys (SAAs), which comprise separated solute atoms in metallic matrix, show great potential on circumventing scaling relationships.[23,26,27] meanwhile, the interaction between the solute atoms and matrix can modify their electronic structure,[26,28,29] leading to a

suitable adsorption energy for hydrogen. Consequently, constructing Ru-based SAAs opens a new avenue towards high HER performance.

Herein we reported the synthesis of RuAu SAAs through a laser ablation in liquid (LAL) technique, which possesses strong quenching effect so as to fabricate metastable nanostructures with novel properties.[30,31] We choose Au as the alloying element on the basis of the following considerations: first, Au is known as an inert metal with weak hydrogen adsorption thus can counteract the strong hydrogen adsorption of Ru matrix. Second, the immiscibility between Au and Ru may create a unique geometric and electronic structures in RuAu SAAs.[32,33] Finally, chemically inert Au favors long-term durability during the reaction. As such, the as-prepared RuAu catalyst exhibits a low overpotential, 24 mV@10 mA cm^{-2}, which is much lower than Pt/C (46 mV@10 mA cm^{-2}) in alkaline media. Moreover, the turnover frequency (TOF) of RuAu SAAs is 3 times that of the Pt/C catalyst. Density functional theory (DFT) computation reveals that the high performance originates from the relay catalysis of Ru host (for water dissociation) and Au dopant (for hydrogen evolution). To the best of our knowledge, this is the first report on the synthesis of RuAu SAAs with outstanding HER performance in alkaline media. Furthermore, the idea of the mixing immiscible metallic elements by LAL can be facilely extended to other material systems for engineering novel catalysts with extraordinary properties.

2. Results and discussion

The synthetic route is schematically illustrated in **Figure 1a**. First, a Ru target was immersed in an aqueous solution containing 0.2 mM HCl and $HAuCl_4$ with varied concentration (0.1, 0.2, 0.3 and 0.5 mM), and the corresponding products are designated as Ru, RuAu-0.1, RuAu-0.2, RuAu-0.3 and RuAu-0.5 SAAs. A nanosecond laser with a pulse width of 7 ns was employed to irradiate the Ru target, leading to the vaporization of the solid target, thermal decomposition of $HAuCl_4$, and formation of SAAs during the subsequent fast quenching.

Figure 1b presents a typical transmission electron microscopic (TEM) image of RuAu-0.2 nanoparticles with an average size of 8 nm (inset of **Figure 1b**). Energy dispersive spectrometer (EDS) elemental mapping analysis indicates that Ru and Au atoms are distributed evenly throughout the particle (**Figure 1c-f**). High-angle annular dark field-scanning transmission electron microscopy (HAADF-STEM) analysis gives more details on the elemental distribution. As shown in **Figure 1g**, Au atoms (in red circles) show higher contrast due to their large atomic number, and disperse individually in Ru host. The magnified HAADF-STEM images (**Figure 1h, Figure S1**) reveal clearly that Au atoms occupy the positions of Ru atoms, which is further proved by the profile of integrated pixel intensity along the white solid line in **Figure 1h**. For comparison, the HAADF-STEM of Ru is displayed

in **Figure S2**. To confirm the scattered distribution Au atoms in the single atom alloys, X-ray absorption near-edge structure (XANES) and extended X-ray absorption fine structure (EXAFS) analyses were conducted for RuAu-0.2, Au foil, and Ru foil. As shown in the XANES spectra, Au L_3-edge and Ru K-edge of RuAu-0.2 are similar to these of Au and Ru foils, respectively **(Figures S3a** and **S3b)**, indicating the metallic state of Au and Ru atoms. RuAu-0.2 exhibit a prominent peak at ~2.2 Å in the Au-L_3 edge k^3-weighted EXAFS spectra in k-space (**Figure S3c**), which is different from the Au-Au characteristic peak (~2.7 Å) of Au foil, and could be attributed to the Ru-Au bonds, thus revealing the dispersion of isolated Au atoms in Ru nanoparticles. Moreover, the Ru-Ru bond length of RuAu-0.2 is same with that of Ru foil (**Figure S3d**). By tuning the concentration of $HAuCl_4$, RuAu SAAs with different contents of Au are prepared (**Figure S4**). As illustrated by the inductively coupled plasma (ICP) results shown in **Table S1**, the Au contents for RuAu-0.1, RuAu-0.2, RuAu-0.3 and RuAu-0.5 SAAs are 9.91 at.%, 15.35 at.%, 21.06 at.%, 36.53 at.%, respectively. X-ray diffraction (XRD) patterns provide further evidence on the increase in Au content. As shown in **Figure S5**, the diffraction peaks of RuAu-0.1 and RuAu-0.2 match well the hexagonal close-packed (hcp) phase of Ru (PDF no. 70-0274), and no diffraction peaks related to Au are detected. While for RuAu-0.3 and RuAu-0.5, diffraction peaks of Au (220) are found in the XRD patterns. Correspondingly, Au clusters emerge in RuAu-0.5 SAAs (**Figure S6)**. These results illustrate that there is an upper limit for Au atoms dissolved in RuAu SAAs.

The HER performance of RuAu-0.2 SAAs is tested in 1 M KOH solution. For comparison, the electrocatalytic properties of pure Ru, commercial Pt/C and Au/C (20 wt%) are also tested under the same conditions. The iR compensated linear sweep voltammetry (LSV) polarization curves illuminate that RuAu-0.2 has the highest catalytic activity among the four catalysts (**Figure 2a**). The overpotential at 10 mA cm^{-2} for RuAu-0.2 is as low as 24 mV, being 22 and 34 mV lower than that of Pt/C and Ru, respectively. The Tafel slope of RuAu-0.2 is 37 mV dec^{-1}, quite lower than that of Ru (68 mV dec^{-1}), Au (155 mV dec^{-1}) and Pt (49 mV dec^{-1}) (**Figure 2b**). Besides, the electrochemical impedance spectra (EIS) illustrate that the charge transfer resistance of RuAu-0.2 is even smaller than Pt/C, suggesting more efficient electron transfer at the interface of RuAu-0.2 and electrolyte **(Figure 2c).** The number of active sites was estimated by copper underpotential deposition (Cu-upd) method (**Figure S7**), and then was adopted to calculate TOF.[34, 35] As shown in **Figure 2d**, RuAu-0.2 exhibits an exceedingly high TOF of 2.18 s^{-1} at the overpotential of 50 mV, which is 3 times that of Pt/C, and 3.6 times that of Ru/C. The performance of RuAu-0.2 is the highest in alkaline media among the recently reported metallic catalysts (**Table S2**). Moreover, Au content can influence HER performance of SAAs remarkably, and RuAu-0.2 exhibits the best catalytic performance among RuAu SAAs with various gold contents (**Figure S8**).

The electrocatalytic stability of RuAu-0.2 is evaluated by a long-term cycling test. As shown in **Figure 2e**, there is only a negligible increase (about 2 mV) in the overpotential of RuAu-0.2 after 1000 cycles. In comparison, the overpotential of Pt/C increases by about 10 mV. The electrochemical stability of RuAu-0.2 is further proved by the chronoamperometry test (**Figure 2f**). After 10 h continuous testing, the catalytic current density shows a slight drop of 8%. In addition, no obvious change was found in the structure (**Figure S9**) and composition (**Figure S10**) after the durability test. Moreover, the Faradaic yield keeps 100% during the durability test, indicating the current observed is fully attributed to HER (**Figure 2f**).

We further carried out X-ray photoelectron spectroscopy (XPS) analysis on RuAu SAAs to reveal their electron structure (**Figures 3a** and **S11**). The Ru $3d_{5/2}$ peak (280.7 eV) of RuAu-0.2 shifts towards high binding energy by 0.18 eV as compared with that of pure Ru.[36, 37] Meanwhile, the Au 4f peak shows a negative shift by 0.2 eV after alloying (**Figure 3b**). These opposite shifts are ascribed to electron transfer from Ru to Au, which was further confirmed by Bader charge analysis shown in **Figures 3c** and **3d**. Interestingly, the extents of peak shift of RuAu-0.3 and RuAu-0.5 are smaller than that of RuAu-0.2 (**Figures S11** and **S12**), indicating the phase separation of Au particles from the Ru host in the alloys with higher Au contents. The change of electronic structures for Ru and Au will lead to the

change of their d-band filling. For Ru, the d-band filling decreases due to the loss of electrons, while for Au atoms, the d-band filling increases after the gain of electrons from Ru. Both of the changes could influence the absorption of H according to the d-band center theory[38].

Next we performed DFT calculations both from the thermodynamics and kinetics aspects to explore the origin of the superior HER activity of RuAu SAAs. RuAu(001), Ru(001) and Pt(111) facets, commonly adopted for theoretical studies,[17,18,39,40] were modeled to represent RuAu-0.2 SAAs, Ru and Pt catalysts, respectively (**Figure S13**). In alkaline medium, HER usually experiences three steps. The first step involves the adsorption of water molecules on catalyst surface,

$$H_2O + * \rightarrow H_2O* \quad (1)$$

then the adsorbed water molecule dissociates to supply hydrogen atoms. Based on the Tafel slope of SAAs, the HER should follow Volmer-Heyrovsky process:[19]

$$H_2O* + e^- \rightarrow H* + OH^- \text{ (Volmer reaction)} \quad (2)$$

$$H_2O + e^- + H* \rightarrow H_2 + OH^- \text{ (Heyrovsky reaction)} \quad (3)$$

From the thermodynamic aspect, for water adsorption (step 1), the binding energies of H_2O on Pt(111), Ru(001), and RuAu(001) facets were determined as 0.173, 0.042, 0.025 eV,

respectively, and the optimal binding sites are the Ru atoms around Au atoms on RuAu(001) facets (**Figure S14**).

For Volmer reaction (step 2), the driving force (Gibbs free energy change, ΔG_T) increases in the order of Pt (111) (0.53 eV), RuAu(001), (0.09 eV), and Ru(001) (-0.60 eV), while for Heyrovsky reaction (step 3), the driving force increases in an opposite order, namely, Ru(001) (0.60 eV), RuAu(001) (-0.09 eV) and Pt (111) (-0.53 eV) (**Figures 4a** and **4b**). On Pt(111), a high energy barrier (0.53 eV) must be overcome in Volmer step due to the poor adsorption of H_2O (**Figure S14**), and on Ru(001), an energy barrier of 0.60 eV appears in Heyrovsky step due the excessively tight hydrogen adsorption (**Figure S15**). In contrast, the energy barrier for RuAu(001) plane is merely 0.09 eV (in Volume step) due to the appropriate H adsorption on Au sites and OH^- adsorption on Ru sites. The excellent adsorption capability of Au sites is proved by the performance of RuAu SAAs in an acidic solution which merely involves the adsorption of hydrogen. As shown in **Figure S16**, pure Au or pure Ru nanoparticles display very poor HER performance, once Ru matrix was doped with Au atoms, the HER performance of the RuAu nanoparticles was remarkably improved, and the higher Au content, the better HER performance. This phenomenon can be rationalized as below: in RuAu SAAs, Au atom gains electrons from Ru matrix, leading to the increase in the filling of Au d-band, as verified by XPS results and Bader charge analysis

(Figure 3). The change of electronic structure promotes the interaction between Au atom and intermediate, thus makes the Au atom as the active site for HER.

Moreover, Ru sites in RuAu(001) show a weaker attraction to OH^- radicals than Ru(001) (**Figure S17**), which facilitates the regeneration of active site and thus accelerates the whole HER process. In consideration of all the above three steps, RuAu (001) plane exhibits appropriate adsorption of water molecules (on Ru atoms) and hydrogen atoms (on Au atoms). Hence, from the thermodynamic point of view, RuAu (001) should be the best HER catalyst in alkaline solution among the three models.

In terms of kinetic, DFT calculations were made to investigate the activation energies for water dissociation (ΔG_B). As shown in **Figures 4a, 4b** and **S18**, RuAu(001) and Ru(001) exhibit lower activation energies (0.98 eV and 0.79 eV, respectively) as compared with Pt(111) (1.05 eV), indicating the dissociation of H_2O on RuAu(001) and Ru(001) facets are easier than Pt(111) facet. The higher energy barrier on RuAu(001) than that on Ru(001) should be attributed to the electronic structure change caused by Au alloying. In order to exclude the occasionality of a certain facet, we also calculated the case of RuAu(101) plane (**Figures S19** and **S20**). After being doped with Au single atom, the RuAu(101) plane shows similar thermodynamic and kinetics behaviors with RuAu(001) plane.

Based on the above, the high HER performance of RuAu SAAs can be understood as below. The electron transfer from Ru to Au atoms in RuAu SAAs leads to positive Ru atoms and negative Au atoms which are favorable to adsorb water molecules and hydrogen atoms, respectively, thus accelerating the whole HRE process in alkaline conditions. The details are shown in **Figures 5a-5d.** Firstly, water molecules are captured by the Ru atoms around Au atoms which possess higher adsorption energy than other Ru atoms and Au atoms (**Figure 5a**). The adsorbed water molecules then dissociate into H^+ and OH^- radicals, the released H^+ ions are immediately captured and reduced by the adjacent Au atom with appropriate adsorption energy (**Figure 5b**). Simultaneously, another water molecule is activated on a Ru atom around the Au atom (**Figure 5c**), then reacts with the adsorbed H atom on Au site giving rise to hydrogen molecule following the Heyrovsky reaction (**Figure 5d**). Eventually, the hydrogen molecule desorbs from Au site to close the hydrogen evolution circle. Obviously, there exists a relay catalysis in RuAu SAAs, namely, Ru atoms work as the first active site to capture and split water molecules, subsequently, Au atoms act as the second active site for absorption of protons and desorption of H_2 gas, as such, the RuAu SAAs achieve a perfect balance on the adsorption of water molecule and proton, thus realizing ultralow overpotential for HER in alkaline media.

To test the universality of synthesis of SAAs by LAL, RuAg SAAs were prepared by the same procedure although Ru and Ag are immiscible in solid state. RuAg-0.2, RuAg-0.4, RuAg-0.7 and RuAg-1 were obtained by laser ablation of a Ru target immersed in $AgNO_3$ aqueous solutions with concentration of 0.2, 0.4, 0.7 and 1.0 mM, respectively. TEM observation indicates that the products are homogenous nanoparticles with high crystallinity (**Figure S21a-b**). EDS elemental mapping shows that Ru and Ag are evenly distributed throughout the particle (**Figure S21c-f**). XRD pattern illustrates that silver is mixed with ruthenium at the atomic level to form a homogenous alloy (**Figure S21g**). The HER performance of above catalysts was tested in both basic and acidic media (**Figure S22**). The catalytic activity of RuAg SAAs first increases and then decreases with the increase of the silver content, being similar to RuAu SAAs. The lowest overpotentials at 10 mA cm^{-2} in basic and acidic media are 37 and 61 mV, respectively, demonstrating that RuAg SAAs are good HER catalysts under alkaline conditions. Therefore, LAL technique can be applied for the production of various alloy catalysts whose parent metals are immiscible in solid state.

3. Conclusion

We, for the first time, synthesized RuAu single-atom alloys whose parent metals are immiscible by laser ablation in liquid. The RuAu SAAs exhibit outstanding electrocatalytic properties (overpotential 24 mV@10 $mAcm^{-2}$) and high stability in alkaline media. The

conceptually new RuAu SAAs outperform the state-of-art Pt/C catalyst in terms of both performance and price (1/30 of Pt), thus show huge advantage for practical and scalable application. According to experimental data and theoretical calculation, RuAu SAAs accelerate HER in the alkaline media by relay catalysis, namely, Ru atoms capture and split water molecules, and Au atoms absorb protons and promote the formation of hydrogen gas, as such, the RuAu SAAs realize an ultralow overpotential for HER in alkaline media. More importantly, our work demonstrates that laser ablation in liquid is an effective strategy on producing novel single atom alloys which show exciting properties for catalytic application.

4. Experimental Section

Material Synthesis: The Ru target (5 mm thick, purity quotient 99.99%) was polished and washed 3 times with ultra-pure water, then immersed into 20 ml $HAuCl_4$ aqueous solutions in an 80 mL breaker. The concentration of the $HAuCl_4$ aqueous solutions were fixed at 0.1 mM, 0.2 mM, 0.3 mM and 0.5 mM, respectively. For comparison, 0.2 mM HCl were selected as the reference. A nanosecond pulsed Nd:YAG laser with wavelength 1064 nm, repetition frequency 15 Hz and pulse width 7 ns was adopted to ablate the target immersed in the beaker for 30 min. The suspension was centrifuged and washed with deionized water for

four times, subsequently dried by lyophilization. 5 mg as-obtained powders were then mixed 20 mg carbon black to serve as HER catalysts.

Materials characterization: The morphology and structure were determined by JEOL ARM-200F equipped with a cold field emission gun and a Cs corrector (CEOS) for probing lenses at the operation voltage of 200 kV. EDS mapping were carried out on a JEOL JEM-2100F transmission electron microscope. XRD characterization was performed on a Siemens-Bruker D5000 X-ray diffractometer with Cu Kα radiation. The X-ray-absorption spectra were recorded using the synchrotron radiation provided by the DCI storage ring at the beamline 12 BM of Advanced Photon Source (APS) in Argonne National Laboratory. The synchrotron radiation was produced by a storage ring operated with 1.85 GeV positrons and with a maximum beam intensity of ca. 300 mA. The measurements were performed with the EXAFS III spectrometer that uses a double crystal silicon (311) monochromator and were carried out in the transmission mode with ionization chambers in front and behind the absorber. Analysis of the XAS spectra was carried out by using Athena and Artemis software packages. The XPS data for surface states of the samples were collected by the X-ray photoelectron spectroscopy (XPS, ESCALAB 250 Xi) with an ESCALAB 250Xi spectrometer (Thermo Fisher Scientific) by using an Al Kα (1486.6 eV) excitation source. The relative

content of gold and ruthenium is determined by inductively coupled plasma mass spectrometry (ICP-MS, Agilent 7700X).

Electrochemical characterization: Electrochemical measurements were performed in a three-electrode electrochemical cell on a CHI 600E electrochemical workstation in N_2-saturated 1 M KOH and in 0.5 M H_2SO_4 electrolytes. 5 mg the catalyst was dispersed in 1 ml water containing 40 μL Nafion. Then 4 μL of the aqueous dispersion was transferred onto a glassy carbon electrode with a 3 mm diameter serving as a working electrode. The reference electrode was a saturated calomel electrode (SCE) and the counter electrode was a graphite rod. All potentials were converted to reversible hydrogen electrode (RHE) by using pure hydrogen calibration (**Figure S23**). The polarization curves were recorded with a scan rate of 5 mV s^{-1} and all data were corrected with the iR correction. The electrochemical impedance spectroscopy (EIS) was tested under -0.03 V in 1 M KOH and -0.05 V in 0.5 M H_2SO_4 with the frequency from 0.1 to 10^6 Hz. The turnover frequency (TOF) was calculated by copper underpotential deposition (Cu-upd) method following the standard equation:[17,18,34,35]

$$TOF = \frac{i}{2Fn} \quad (1)$$

$$n = \frac{Q_{Cu}}{2F} \quad (2)$$

where i is the current (mA) at η = 50 mV; n (mmol) the mole number of the active metal atoms, F the Faraday constant (96485 C mol^{-1}), Q_{Cu} the UPD copper stripping charge. The coefficient 1/2 in **Equation (2)** is because it takes 2 electrons to form a hydrogen molecule.

The Q_{Cu} is measured under the deposition potential of copper (Cu^{2+}/Cu) is ~ 0.23V vs. RHE.[35] First, the electrode was cycled between 0.26 and 0.9 V for several times in 0.25 M H_2SO_4. Then, the electrode was transferred to the electrolyte containing 0.25 M H_2SO_4 and 10 mM $CuSO_4$ and being saturated with N_2. For our alloy, the anodic peak is about 0.39 V, which is attributed to the Cu stripping peak,[34,35] thus the Q_{Cu} of RuAu-0.2 is 1.2mC. While the Q_{Cu} of Pt and Ru is 1.1mC and 0.86mC, respectively. The number of active metal atoms n can be calculated through the **Equation (2)**. Then the TOF can be obtained according to the **Equation (1)**.

The catalytic durability was performed at a constant current density of 10 mA cm^{-2}. Accelerated durability test was performed by 1000 potential cycles in 1 M KOH solution from 0.14 to −0.26 V (versus RHE). Faradaic efficiency was tested at - 0.03 V vs reversible hydrogen electrode.

Supporting Information

Supporting Information is available from the Wiley Online Library or from the author.

Acknowledgements

This work was supported by the Natural Science Foundation of China (Nos. 51871160, 51671141, 51471115, 51402084 and 51471079).

References

[1] L. Schlapbach, *Nature* **2009**, *460*, 809.

[2] M. S. Dresselhaus, I. L. Thomas, *Nature* **2001**, *414*, 332.

[3] Z. Chen, R. Wu, Y. Liu, Y. Ha, Y. Guo, D. Sun, M. Liu, F. Fang, *Adv. Mater.* **2018**, *30*, 1802011.

[4] W. Hao, R. Wu, R. Zhang, Y. Ha, Z. Chen, L. Wang, Y. Yang, X. Ma, D. Sun, F. Fang, Y. Guo, *Adv.Energy Mater.* **2018**, *8*, 1801372.

[5] F. Li, G. Han, H. Noh, Y. Lu, J. Xu, Y. Bu, Z. Fu, J. Baek, *Angew. Chem. Int. Ed.* **2018**, *57*, 14139.

[6] J. Greeley, T. F. Jaramillo, J. Bonde, I. B. Chorkendorff, J. K. Norskov, *Nat. Mater.* **2006**, *5*, 909.

[7] J. D. Benck, T. R. Hellstern, J. Kibsgaard, P. Chakthranont, T. F. Jaramillo, *ACS Catal.* **2014**, *4*, 3957.

[8] J. Durst, A. Siebel, C. Simon, F. Hasch´e, J. Herranz, H. A. Gasteiger, *Energy Environ. Sci.* **2014**, *7*, 2255.

[9] T. R. Cook, D. K. Dogutan, S. Y. Reece, Y. Surendranath, T. S. Teets, D. G. Nocera, *Chem. Rev.* **2010**, *110*, 6474.

[10] M. G. Walter, E. L. Warren, J. R. McKone, S. W. Boettcher, Q. X. Mi, E. A. Santori, N. S. Lewis, *Chem. Rev.* **2010**, *110*, 6446.

[11] P. J. Rheinländer, J. Herranz, J. Durst, H. A. Gasteiger, *J. Electrochem. Soc.* **2014**, *161*, F1448.

[12] Z. F. Huang, J. Song, K. Li, M. Tahir, Y. T. Wang, L. Pan, L. Wang, X. Zhang, J. J. Zou, *J. Am. Chem. Soc.* **2016**, *138*, 1359.

[13] J. Staszak-Jirkovsky, C. D. Malliakas, P. P. Lopes, N. Danilovic, S. S. Kota, K. C. Chang, B. Genorio, D. Strmcnik, V. R. Stamenkovic, M. G. Kanatzidis, N. M. Markovic, *Nat. Mater.* **2016**, *15*, 197.

[14]R. Ye, Y. Liu, Z. Peng, T. Wang, A. S. Jalilov, B. I. Yakobson, S. H. Wei, J. M. Tour, *ACS Appl. Mater. Interfaces* **2017**, *9*, 3785.

[15] J. Greeley, M. Mavrikakis, *Nat. Mater.* **2004**, *3*, 810.

[16] G. S. Karlberg, *Phys. Rev. B* **2006**, *74,* 153414.

[17]Y. Zheng, Y. Jiao, Y. Zhu, L. H. Li, Y. Han, Y. Chen, M. Jaroniec, S. Z. Qiao, *J. Am. Chem. Soc.* **2016**, *138*, 16174.

[18] J. Mahmood, F. Li, S. M. Jung, M. S. Okyay, I. Ahmad, S. J. Kim, N. Park, H. Y. Jeong, J. B. Baek, *Nat. Nanotechnol.* **2017**, *12*, 441.

[19] P. Jiang, Y. Yang, R. Shi, G. Xia, J. Chen, J. Su, Q. Chen, *J. Mater. Chem. A* **2017**, *5,* 5475.

[20] J. L. Liu, F. R. Lucci, M. Yang, S. Lee, M. D. Marcinkowski, A. J. Therrien, C. T. Williams, E. C. H. Sykes, M. Flytzani-Stephanopoulos, *J. Am. Chem. Soc.* **2016**, *138*, 6396.

[21] P. Wang, F. Chang, W. Gao, J. Guo, G. Wu, T. He, P. Chen, *Nat. Chem.* **2016**, *9*, 64.

[22] W. D. Li, Y. Liu, M. Wu, X. L. Feng, S. A. T. Redfern, Y. Shang, X. Yong, T. L. Feng, K. F. Wu, Z. Y. Liu, B. J. Li, Z. M. Chen, J. S. Tse, S. Y. Lu, B. Yang, *Adv. Mate.* **2018**, 1800676.

[23] J. Su, Y. Yang, G. Xia, J. Chen, P. Jiang, Q. Chen, *Nat. Commun.* **2017**, *8*, 14969.

[24] J. Zhang, P. Liu, G. Wang, P. P. Zhang, X. D. Zhuang, M. W. Chen, I. M. Weidinger, X. L. Feng, *J. Mater. Chem. A* **2017**, *5,* 25314.

[25] F. Li, G. Han, H. Noh, I. Ahmad, I. Jeon, J Baek, *Adv. Mater.* **2018**, *30*, 1803676.

[26] M. T. Greiner, T. E. Jones, S. Beeg, L. Zwiener, M. Scherzer, F. Girgsdies, S. Piccinin, M. Armbruster, A. Knop-Gericke, R. Schlogl, *Nat. Chem.* **2018**, *10*, 1008.

[27] G. Kyriakou, M. B. Boucher, A. D. Jewell, E. A. Lewis, T. J. Lawton, A. E. Baber, H. L. Tierney, M. Flytzani-Stephanopoulos, E. C. H. Sykes, *Science* **2012**, *335*, 1209.

[28] J. Ge, D. He, W. Chen, H. Ju, H. Zhang, T. Chao, X. Wang, R. You, Y. Lin, Y. Wang, J. Zhu, H. Li, B. Xiao, W. Huang, Y. Wu, X. Hong, Y. Li, *J. Am. Chem. Soc.* **2016**, *138*, 13850.

[29] T. Chao, X. Luo, W. Chen, B. Jiang, J. Ge, Y. Lin, G. Wu, X. Wang, Y. Hu, Z. Zhuang, Y. Wu, X. Hong, Y. Li, *Angew. Chem.* **2017**, *129*, 16263.

[30] H. Liu, P. Jin, Y. M. Xue, C. Dong, X. Li, C. C. Tang, X. W. Du, *Angew. Chem. Int. Edit.* **2015**, *54*, 7051.

[31] J. Xiao, P. Liu, C. X. Wang, G. W. Yang, *Progress in Materials Science* **2017**, *87*, 140.

[32]L. E. Chinchilla, C. M. Olmos, A. Villa, A. Carlsson, L. Prati, X. Chen, G. Blanco, J. J. Calvino, A. B. Hungría, *Catalysis Today* **2015**, *253*, 178.

[33] E. P. Maris, W. C. Ketchie, M. Murayama, R. J. Davis, *Journal of Catalysis* **2007**, *251*, 281.

[34] C. L. Green, A. Kucernak, *J. Phys. Chem. B* **2002**, *106*, 1036.

[35] L. Colmenares, Z. Jusys, R. J. Behm, *Langmuir* **2006**, *22*, 10437.

[36] J. Liu, Y. Zheng, D. Zhu, A. Vasileff, T. Ling, S. Z. Qiao, *Nanoscale* **2017**, *9*, 16616.

[37] W. Luo, M. Sankar, A. M. Beale, Q. He, C. J. Kiely, P. C. Bruijnincx, B. M. Weckhuysen, *Nat. Commun.* **2015**, *6*, 6540.

[38] B. Hammer, J. K. Nørskov, *Advances in Catalysis* **2000**, *45*, 71.

[39] J. K. Nørskov, T. Bligaard, A. Logadottir, J. R. Kitchin, J. G. Chen, S. Pandelov, U. Stimming, *J. Am. Chem. Soc.* **2005**, *152*, J23.

[40] P. J. Feibelman, *Science* **2002**, *295*, 99.

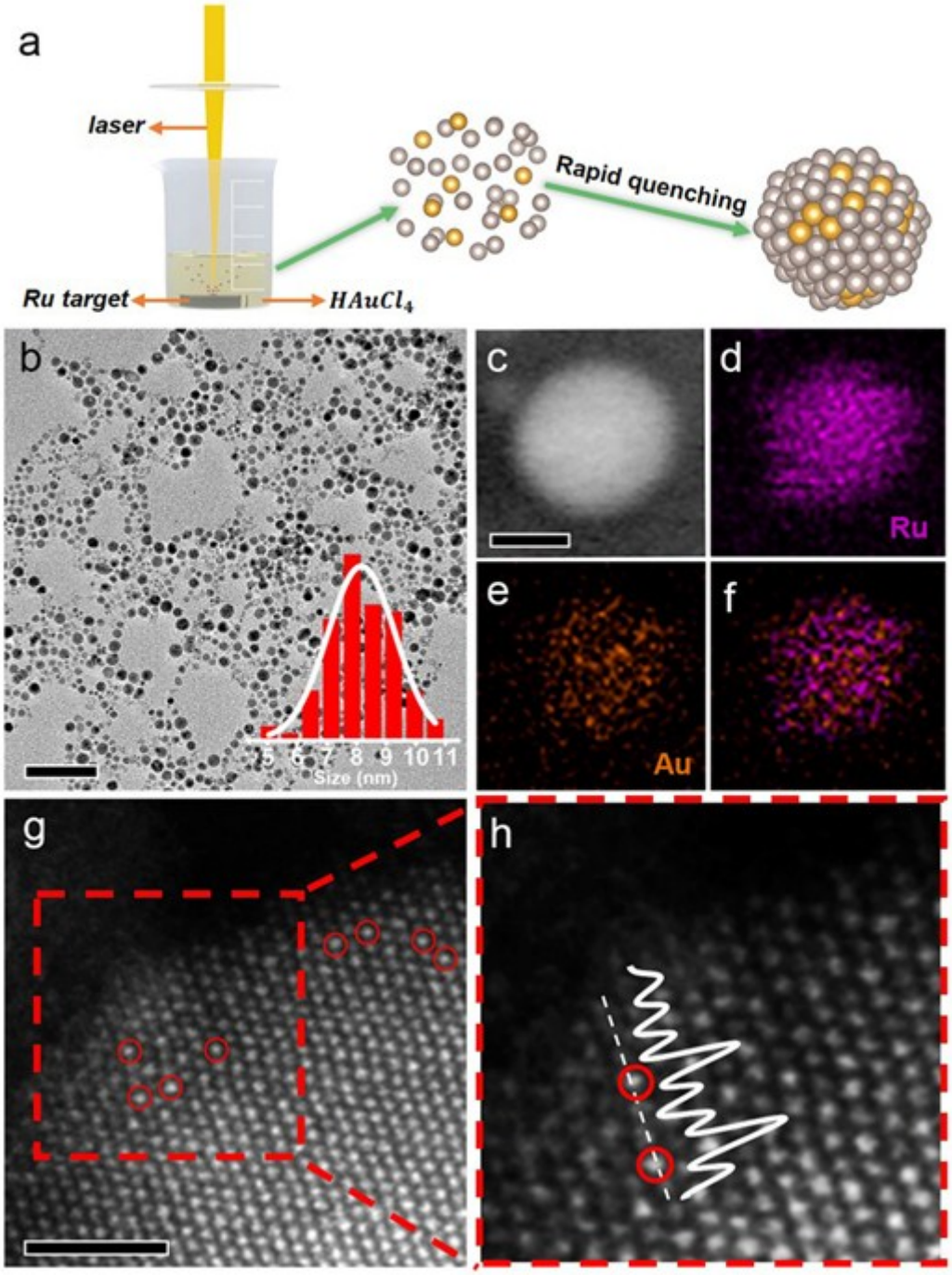

Figure 1. The synthesis of RuAu SAAs and characterizations on RuAu-0.2. (a) The schematic setup of PLAL and the formation process of SAA nanoparticles. (b) TEM of RuAu-0.2. Inset,

particle size distribution. Scale bar, 50 nm. (c-f) HAADF image and elemental mapping of Ru and Au. Scale bar, 5 nm. (g) Atomic-resolution HAADF-STEM image, Au atoms (marked by red circles) are uniformly distributed throughout the particle. Scale bar, 1 nm. (h) Magnified image in red dotted rectangle of (g), Au atoms were marked with red circles. The white solid curve is the integrated pixel intensity along the white dotted line.

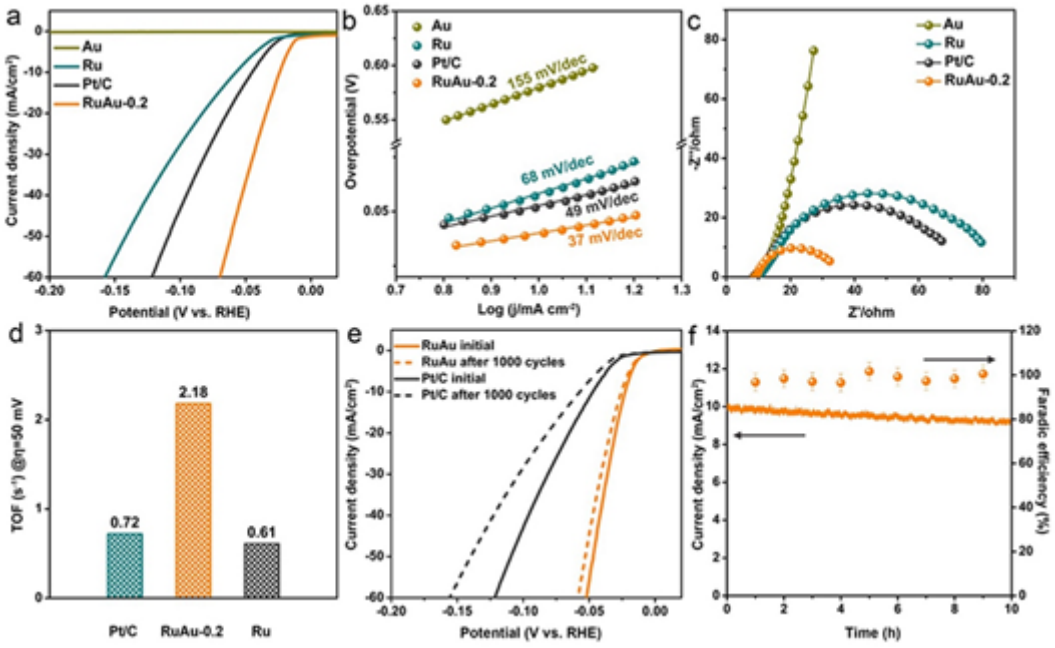

Figure 2. HER activity and stability in 1M KOH solution. (a) Linear sweep voltammetry (LSV) polarization curves (iR compensated) at scan rate of 5 mV s^{-1}; (b) Tafel slopes derived from (a); (c) EIS data; (d) TOF at 50 mV overpotential; (e) Durability test; (f) Chronoamperometric curve at an overpotential of 10 mA cm^{-2} (left) and Faradaic efficiency (right).

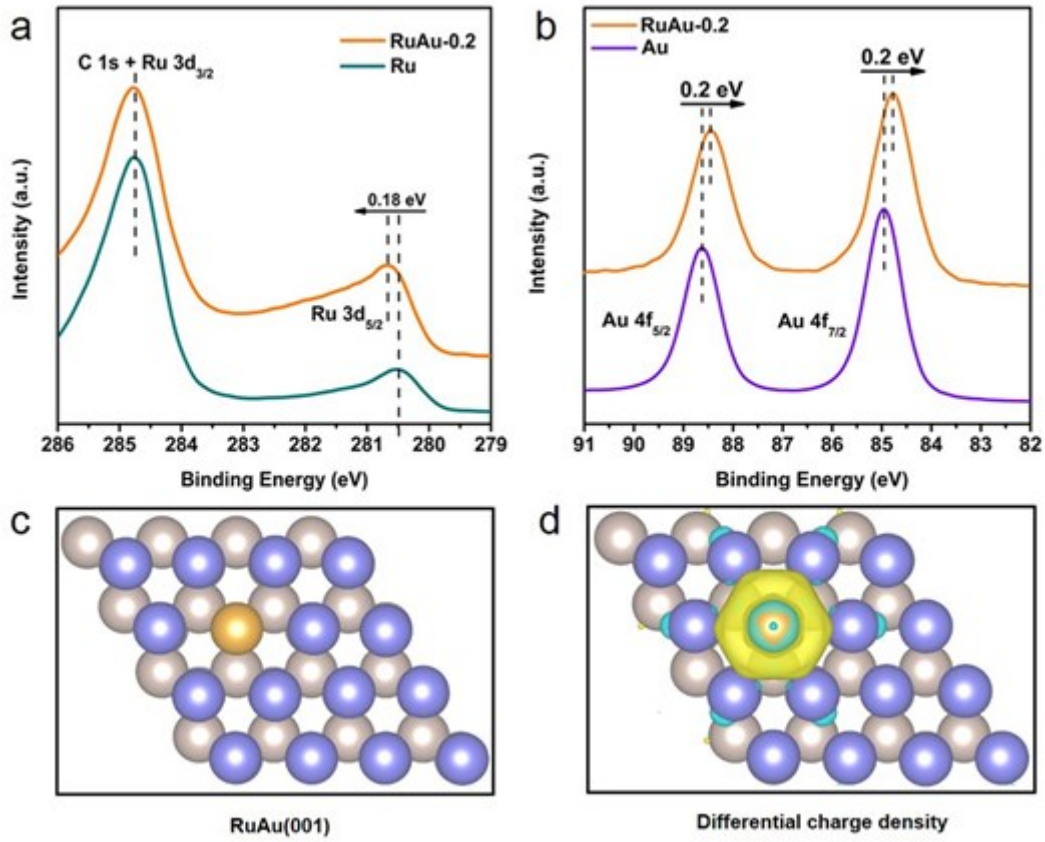

Figure 3. Charge redistribution in RuAu alloy. (a) Ru3d XPS spectra of Ru and RuAu-0.2. (b) Au4f XPS spectra of Au and RuAu-0.2. (c) Atomic model of RuAu (001) surface, yellow ball represents Au atom, and deep blue and silver gray indicate the top and bottom layers of Ru respectively. (d) Differential charge densities of RuAu (001) surface. Yellow and blue contours represent electron accumulation and depletion, respectively.

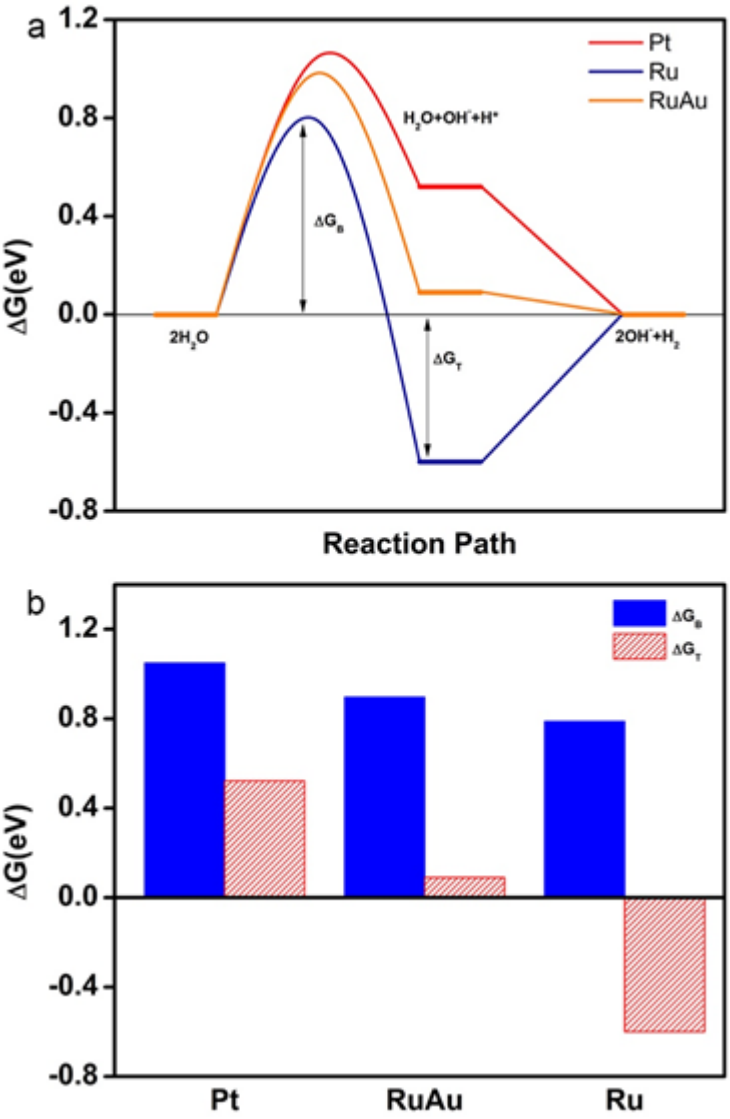

Figure 4. Thermodynamic and kinetics barriers for hydrogen evolution on three catalysts. (a) Gibbs free energy profile of HER on Pt (111), Ru(001) and RuAu(001) surfaces. ΔG_T represents the energy barrier for Heyrovsky reaction. ΔG_B represents the activation energy of water dissociation. (b) ΔG_T and ΔG_B values on the surface of the three models.

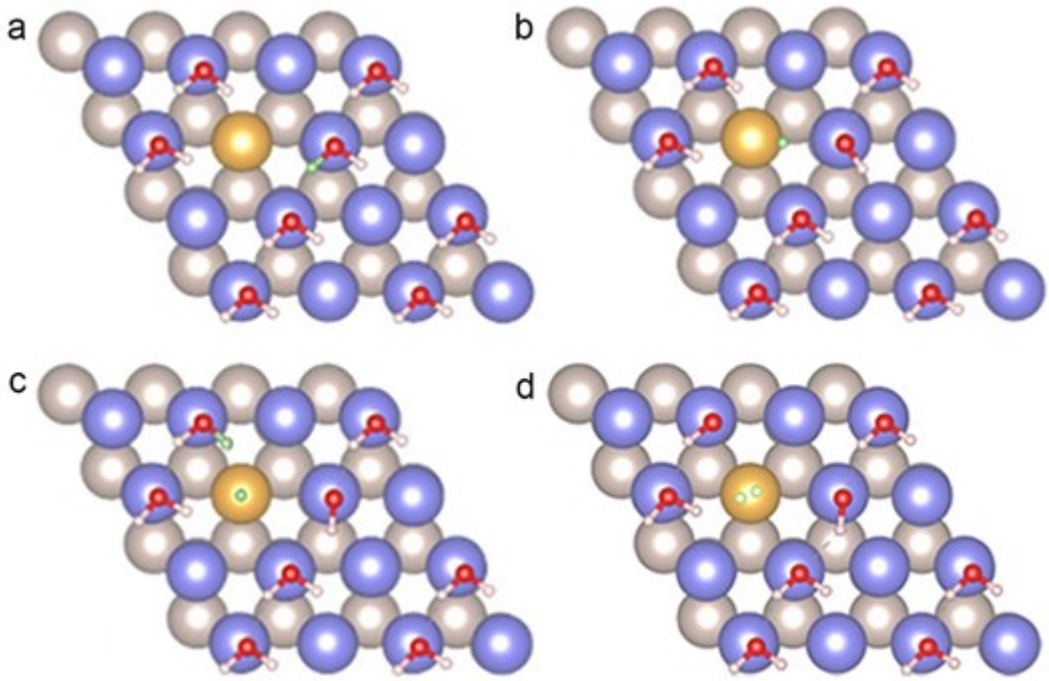

Figure 5. Schematic maps on the hydrogen evolution on RuAu SAAs. (a) H_2O adsorption on Ru atom, (b) H_2O dissociation on Ru atom and H adsorption on Au atom, (c) H_2O activation on the another adjecnt Ru atom, (d) H_2 formation on Au atom. Color codes: deep blue and silver gray represent the top and bottom layers of Ru respectively. Golden and red are Au and oxygen respectively. White and green are hydrogen.

Ruthenium-Based Single Atom Alloy with High Electrocatalytic Activity for Hydrogen Evolution

Keyword

single-atom alloys, hydrogen evolution reaction, pulsed laser ablation, electrocatalyst, synergistic effect

ToC figure ((Please choose one size: 55 mm broad × 50 mm high **or** 110 mm broad × 20 mm high. Please do not use any other dimensions))